Advanced Characterization Methodology to Unravel the Biodegradability of Metal–Organic Framework Nanoparticles in Extremely Diluted Conditions

Ioanna Christodoulou, Gilles Patriarche, Christian Serre, Cédric Boissiére, Ruxandra Gref, Gref Ruxandra

Advanced Characterization Methodology to Unravel the Biodegradability of Metal−Organic Framework Nanoparticles in Extremely Diluted Conditions

Ioanna Christodoulou,* Gilles Patriarche, Christian Serre, Cédric Boissiére, and Ruxandra Gref*

INTRODUCTION

Engineered drug nanocarriers are gaining increasing interest in the treatment of severe diseases such as cancer and resistant infections by protecting the incorporated drugs and ferrying them to the target sites. Since the first design of a controlled-release drug delivery system,[1] a great variety of nanoparticles have been developed and proposed as potential candidates to improve the drug bioavailability and reduce toxic side effects.[2] Recently developed nanosized porous metal−organic frameworks (nanoMOFs) showed high potential as drug carriers due to their important drug payloads, versatility in terms of composition and pore sizes, and convenient surface functionalization.[3−5] In particular, the biocompatible iron carboxylate nanoMOFs have drawn great attention thanks to their biodegradability and lack of *in vivo* toxicity.[6−8]

One of the most studied nanoMOFs in the field of biomedical applications is the mesoporous iron trimesate MIL-100(Fe) (MIL stands for Materials of the Institute Lavoisier) that is built from the assembly of trimers of iron octahedra and trimesate ligands, leading to mesoporous cages delimited by microporous windows. Indeed, nanoparticles of this MOF or nanoMOFs were capable not only of encapsulating a variety of challenging drugs with high payloads and yields close to 100% but also of releasing the drugs often in a controlled manner.[9−12] Some of the most important features of these nanoMOFs are their biodegradability and their in vitro[13−15] and *in vivo* biocompatibility.[6,7,16,17] Nanoparticles of MIL-100(Fe) are chemically stable in aqueous and ethanolic solutions but undergo degradation upon incubation in biological media. Once the nanoparticles are in contact with phosphate-buffered saline (PBS), phosphate ions from the suspension media diffuse inside their pores and coordinate

strongly with the iron metal sites, substituting the organic ligands and leading to a progressive disassembly of the crystalline MOF structure.[3,18−20] Recently, micron-sized MIL-100(Fe) particles were studied to gain a better understanding of their degradation mechanism.[19] Interestingly, the particles were degraded in PBS without any significant size modifications. It was found that degradation was initiated by the diffusion of phosphate ions from PBS into the matrix and that an inorganic shell made of iron phosphate was progressively formed around a dense crystalline core of MIL-100(Fe), leading to a passivation of the surface, slowing the degradation of the particles. The degradation of the MIL-100(Fe) was also studied in PBS enriched with bovine serum albumin (BSA).[18] BSA is the most abundant protein in the bloodstream with a molecular weight of approximately 66 kDa and dimensions of (140 × 40 × 40 Å).[21] This bulky macromolecule was unable to penetrate inside the MOFs' porosity but instead adsorbed at the MOFs' surface, forming a negatively charged protein corona. In the presence of BSA, the detachment of the MOFs' constitutive trimesate ligands was slightly reduced, but the mechanism of degradation was not explored. More recently, it was shown that in the same release medium enriched in BSA, nanosized MIL-100(Fe) decorated with Fe_2O_3 maintained their global morphology during degradation, without size changes.[22]

In addition, the pH of the degrading media plays a key role in the degradation of the nanoMOFs. *In vivo* studies showed that they possess unique pH-responsive properties. Once injected into the bloodstream, nanoparticles of MIL-100(Fe) immediately aggregated at neutral pH and, thus, preferentially accumulated in the lungs where they released their drug content to eradicate the tumor as a consequence of the passive lung targeting.[23] Because of surface degradation, they eventually disassembled and were well tolerated *in vivo*.

In vivo studies are crucial to assess the cytotoxicity and biodistribution of nanoMOFs in living organisms. Yet, these studies are complex as multiple phenomena occur simultaneously inside the body, hampering the deeper understanding of the degradation mechanism of the nanoMOFs. Conversely, in vitro conditions do not mimic the extreme diluted conditions corresponding to nanoMOF injection into the bloodstream. More generally, depending on the studied species, different amounts of nanoparticles are injected, and blood volumes can differ on a large scale (for example, the volume of human blood is around 5 L, whereas in animal tests, volumes can reach around 200 mL for rats and only 5 mL for mice). Therefore, depending on the experimental setup, when nanoMOFs are injected into the bloodstream, they can experience extreme diluted conditions, which can, in turn, tremendously affect their degradation kinetics.

It is worth mentioning that the experimental conditions are also very different in in vitro investigations of nanoMOF degradation.[24,25] Degradation and drug release are typically monitored with a nanoMOF concentration in the range of 0.5−1 mg mL^{-1}.[24] Conversely, in the case of stability and degradation studies followed by dynamic light scattering (DLS) measurements, the typical concentration is only 0.1 mg mL^{-1}.[25] As a result, sometimes inconsistent degradation kinetic data are reported according to the experimental conditions. In addition, the investigation of nanoMOF degradation using microscopy or chromatography is complicated by the necessary steps (centrifugation, washings, and dilutions) commonly required before the measurements. To the best of our knowledge, no study has yet addressed the degradation of nanoMOFs under extremely diluted conditions, which they can experience when administered *in vivo* in humans.

To overcome these limitations, in situ ellipsometry was used here to study nanosized MIL-100(Fe) degradation in real time to gain a better understanding of their behavior under extremely diluted conditions. Ellipsometry is an optical technique based on the measurement of changes in polarization upon reflection or transmission for the investigation of the dielectric properties of the studied material. Thus, changes in the nanoMOF optical properties arising from chemical transformations upon degradation can be followed over time. The main benefit of in situ ellipsometry is that it allows the study of very diluted conditions. In addition, it enables attenuation of the concentration gradients at the surfaces of the nanoparticles to get accurate data. Furthermore, the geometry of the investigation system is fixed so that artifacts which occur due to the possible nanoMOF aggregation cannot alter data. Last but not least, in situ ellipsometry presents a very good temporal resolution, allowing fast and precise measurements, even at early times.

Some of us reported for the first time the use of in situ ellipsometry to study the dissolution of hybrid organosilica nanoparticles in PBS at different temperatures and far from the saturation conditions.[26] It was found that the nanoparticle chemical composition was one of the main factors affecting the degradation kinetics. In a more recent study, the same authors prepared coated mesoporous silica-based films for in situ ellipsometry analysis in PBS with or without BSA.[27] The dissolution rate of silica nanoparticles was mainly controlled by their freely accessible surface area, which regulated the accessibility of the diffused ions in the internal porosity of the particles.

Here, we propose for the first time an in situ analysis of the degradation mechanism of nanoMOFs using spectroscopic ellipsometry (SE). Nanoparticles of around 50 nm of MIL-100(Fe) were synthesized at room temperature (RT) to allow one to obtain films of optical quality by dip-coating. First, the film's thickness was determined at RT by conventional SE, and then film stability was evaluated in water and PBS at 37 °C. Then, degradation was studied as a function of the pH of the degrading medium in the presence or absence of BSA to assess its contribution to the mechanism. These studies were completed with ex situ investigations of morphology and composition using high-angle annular dark-field scanning transmission electron microscopy (STEM-HAADF) coupled with energy-dispersive X-ray spectroscopy (EDX) to monitor the crystalline organization of the MOF and map their elemental distribution. This required the use of larger-sized nanoMOF particles (140 nm) prepared through a microwave (MW)-assisted route. Finally, the release of the MOF constitutive ligand followed, and it showed that the size of the nanoparticles did not affect their degradation kinetics. The main objective of this study is to compare ex situ and in situ techniques to better understand the degradation mechanism of nanosized MIL-100(Fe) under both diluted and nondiluted conditions for a better vision of their design as therapeutic vectors.

EXPERIMENTAL METHOD

Materials. All of the reagents and solvents were purchased from commercial sources and used without any further purification.

Iron(III) nitrate nine-hydrate [$Fe(NO_3)_3{\cdot}9H_2O$] (Sigma-Aldrich), iron(III) chloride hexa-hydrate (98%, Alfa Aesar, France) and 1,3,5-benzene tricarboxylic acid (BTC or trimesic acid) (Sigma-Aldrich) were used for the synthesis of nanoMOFs. Dulbecco's phosphate-buffered saline (DPBS 1×, pH 7.4) was purchased from Thermo Fisher Scientific. It contains 1.47 mM KH_2PO_4, 8.59 mM $Na_2HPO_4{\cdot}7H_2O$, 137 mM NaCl, and 2.66 mM KCl. KH_2PO_4, Na_2HPO_4, NaCl, and KCl (Sigma-Aldrich) were used for the preparation of PBS (pH = 5.4). BSA was purchased from Sigma-Aldrich. Absolute EtOH was purchased from Thermo Fisher Scientific. Milli-Q water (resistivity, 18.2 MΩ cm) was obtained from a Millipore apparatus equipped with a 0.22 μm filter. Silicon substrates were purchased from SolGelWay, Paris, France. 200-mesh copper grids covered with a pure carbon membrane were purchased from Ted Pella.

Synthesis of NanoMOFs. Nanosized MIL-100(Fe) was synthesized by following two pathways. First, nanoparticles with mean diameters of around 50 nm were synthesized from a mixture of 0.25 g of trimesic acid, 0.72 g of $Fe(NO_3)_3{\cdot}9H_2O$, and 90 mL of water, which were mixed in a round-bottom flask at RT under stirring for 48 h. The synthesized particles were recovered by centrifugation (14.000*g*, 15 min) and purified by washing twice with distilled water and twice in absolute EtOH.[28] The nanoparticles were stored as suspensions in absolute EtOH until their final use. They are named nanoMOFs (RT).

Second, larger-sized nanoMOFs (140 nm) were obtained using a microwave-assisted hydrothermal synthesis, as previously reported.[29,30] A mixture of iron chloride (2.425 g) and trimesic acid (0.846 g) was placed in Teflon-sealed autoclave reactors with 20 mL of deionized water and heated for 6 min at 130 °C under stirring. The applied power was 800 W (Mars-5, CEM, US). The nucleation reaction was stopped by placing the reactors in an ice bath for 10 min. The resulting nanoparticles were recovered by centrifugation (14.000*g*, 15 min) and were purified by washing with absolute EtOH 6 times to remove the residual nonreacted organic acid. A last centrifugation at 2000*g* was performed for 1 min in absolute EtOH to sediment the largest particles and recover the supernatants as a suspension of monodisperse nanoparticles. The synthesized product was stored wet in EtOH until the final use. They are named nanoMOFs (MW).

Characterizations of NanoMOFs. The nanoparticles were characterized before and after degradation under physiological conditions by a set of complementary techniques.

Powder X-ray diffraction (PXRD) analysis was carried out with a D8 Advance Bruker Diffractometer in Debye−Scherrer geometry in the 2θ range of 2−40°. The diffractometer was equipped with a Ge(111) monochromator producing Cu Kα1 radiation (λ = 1.540598 Å) and a LynxEye detector. Infrared spectra were collected using a Nicolet iS5 FT-IR (Thermo Scientific, USA) from 4000 to 400 cm^{-1}. Porosity was evaluated by N_2 sorption isotherms obtained at 77 K by using a Micromeritics Tristar apparatus. Before the analysis, around 30 mg of nanoMOF samples were activated by heating at 150 °C under secondary vacuum for 5 h. The size distribution and the polydispersity of nanoMOFs in suspension were determined by DLS, and ζ-potential measurements were performed using a Malvern Nano-ZS of the Zetasizer Nano series. To do so, nanoparticles from ethanolic suspensions were washed twice with Milli-Q water and finally resuspended in Milli-Q water at a concentration of 0.1 mg mL^{-1}. Experiments were performed in triplicate at 25 °C.

The optical spectra of the nanoMOFs in the form of suspensions and in a dried state were measured using a Varian Cary 300 Bio UV−vis spectrometer equipped with an integration sphere in the diffuse reflectance mode. The release of the trimesate ligand was quantified using a reversed-phase high-performance liquid chromatography (HPLC) system (Waters Alliance e2695 Separations Module, Waters, Milford, MA) equipped with a UV−vis detector (Waters 2998), as previously described.[20] The system was controlled by Agilent software. A SunFire-C18 reverse-phase column (5 μm, 4.6 × 150 mm^2, Waters) was employed. For the analysis of the constitutive ligand, 1,3,5-benzenetricarboxylic acid or BTC, a mobile phase A consisting of a buffer solution (0.04 M, pH 2.5), and a mobile phase B MeOH (50:50) were used. The buffer (phase A) was prepared by dissolving NaH_2PO_4 (2.4 g, 0.02 mol) and Na_2HPO_4 (2.84 g, 0.02 mol) in 1 L of Milli-Q water. The pH was then adjusted to 2.5 with H_3PO_4 (≥85%). The injection volume was 50 μL, and the detection wavelength was set at 225 nm. The column temperature was fixed at 25 °C.

The TEM/STEM studies were performed on a Titan Themis microscope corrected for spherical aberrations on the probe. The microscope was equipped with the "Super-X" analysis EDX system with 4 silicon drift detectors, achieving a solid angle of 0.8 sr. The observations were made at 200 kV with a sufficiently low probe current, i.e., around 40−50 pA, so as to not degrade the sample. The STEM−EDX chemical maps are carried out under the same conditions, for an acquisition time of approximately 15−20 min. For the HAADF-STEM image acquisition, the half angle of convergence of the probe was 17 mrad and the collection half angle of the annular dark-field detector was 69 mrad (inner angle) and 200 mrad (outer angle). For the TEM grid preparation, a 2 μL drop of the nanoMOF suspensions was placed on a 200-mesh copper grid.

Thin Film NanoMOF Deposition. For the thin film's formation, the nanoparticles were redispersed in absolute EtOH and centrifuged at low speed (2000*g*, 1 min) to eliminate the largest aggregates. The supernatant containing suspended small aggregates (3.7 mg mL^{-1}) was used for the dip-coating procedure. The ethanolic dispersion of nanoMOFs (RT) was dip-coated at RT on a silicon substrate with a withdrawal speed of 8 mm s^{-1}. Relative humidity was measured at 50%. The films were prepared by double-coating with nanoparticle dispersions after thermal treatment at 130 °C for 5 min. They were characterized by scanning electron microscopy (FEG-SEM Sigma HD, Zeiss), and their thickness and optical properties were determined by SE.

Spectroscopic Ellipsometry. SE experiments were performed using an M2000 spectroscopic ellipsometer equipped with a UV-IR detector in the 193−1690 nm spectral range. The acquisition time was 5 s for each point. Data were analyzed with CompleteEASE software. The imaginary part of the dispersion function of the film was modeled with a single Cody−Lorentz and two Lorentz oscillators in the 300−1000 nm wavelength range.

Ellipsometric analyses at an infrared angle were performed with a MARK II IR-VASE instrument from Woolam within a closed cell flushed with dry air. MOF films deposited onto the silicon wafer were analyzed at a 75° incidence angle. The film thickness and refractive index were determined at 0% relative humidity.

In Situ Ellipsometry. In situ dissolution experiments of nanoMOFs (RT) were performed with a thermostated ellipsometric liquid cell from Linkam. Data were collected every minute at an incidence of 75° using the visible light wavelength range. The ellipsometer acquisition conditions were one measure of 5 s every minute. The experiments were performed at 37 °C, to mimic the body's temperature, and the media in contact with the films (100 mL total volumes) were circulated within the analysis cell at a flow rate of 10 mL min^{-1}. The media used were Milli-Q water and 10 mM PBS containing or not containing BSA. The pH of the PBS medium was acidic (pH 5.4) or neutral (pH 7.4), whereas the concentration of BSA in PBS with a pH value of 7.4 was 3.7% w/v to mimic albumin concentration in human blood.

Data were analyzed with CompleteEASE software. The imaginary part of the dispersion function was modeled with a single Cody−Lorentz oscillator in the 500−900 nm wavelength range.

RESULTS AND DISCUSSIONS

Characterizations of nanoMOFs. MIL-100(Fe) presents a highly ordered mesoporous 3D structure, resulting from the self-assembly of iron trimers with trimesate ligands. This results in a zeotype architecture of an MTN topology composed of two types of interconnected mesoporous cages of 25 and 29 Å (Figure 1 upper panel), the larger cages being accessible through microporous pentagonal and hexagonal

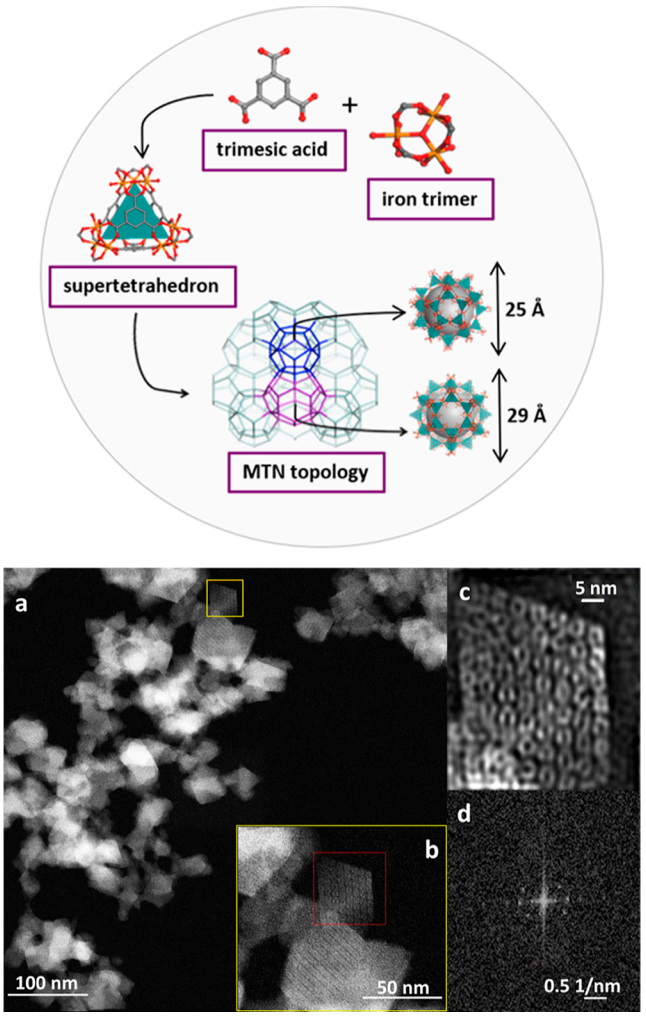

Figure 1. Upper panel: schematic representation of the structure of MIL-100(Fe) obtained by the self-assembly of BTC and iron, forming super tetrahedra and then 3D mesoporous cages of 25 and 29 Å, accessible through microporous pentagonal windows of around 5 Å and microporous hexagonal windows of 8.6 Å. Lower panel: typical STEM-HAADF images of synthesized nanoMOFs (RT). (a) Unprocessed image; (b) magnified image; (c) inverse fast Fourier transform (FFT) filtered HAADF-STEM image, and (d) typical FFT pattern which reveals the crystallinity of the particles.

windows of 5.6 and 8.6 Å, respectively, and the small cages being accessible only through pentagonal windows (Figure 1).

Whatever the synthesis method, crystalline nanoMOFs (RT) and nanoMOFs (MW) were successfully obtained, as demonstrated by a series of complementary investigations. First, due to its ultrahigh image resolution, STEM-HAADF performed on the nanoMOF (RT) sample enabled the direct visualization of its crystalline structure, including its mesoporous cages, as illustrated in Figure 1a–c. A well-faceted octahedral morphology with an average diameter of 60 ± 10 nm is observed, while the crystalline structure of individual particles was indicated by their FFT patterns (Figure 1d). Yet, the ultrasmall nanoMOFs synthesized at RT were prone to aggregate rapidly in aqueous suspensions, as indicated by both SEM and DLS investigations (Figure S1). To overcome this limitation, we also synthesized nanoMOFs (MW) with average sizes of 140 ± 37 nm, measured by STEM-HAADF (Figure S2). Sizes determined by DLS were higher (210 ± 20 nm), but the polydispersity indices were low (0.07). In contrast to nanoMOFs (RT), nanoMOFs (MW) were more stable in aqueous media, possibly because of their lower external surfaces. Both nanoMOFs (RT) and nanoMOFs (MW) exhibited a positive ζ-potential of +26 ± 2 mV at acidic pH (3.5) and a negative ζ-potential of −38 ± 2 mV at pH 7.4, in agreement with previously reported data.[19,22,23]

The synthesized nanoMOFs were further characterized by PXRD, FT-IR spectroscopy, and N_2 porosimetry. PXRD patterns were in agreement with data in the literature, showing the successful synthesis of a highly crystalline product (Figure S3).[30,31] FT-IR spectroscopy allowed for the investigation of the composition of the nanoMOFs. As shown in Figure S4, the two bands at 1640 and 1380 cm^{-1}, corresponding to the asymmetric ν(C−O)s and symmetric ν(C−O)s stretching modes of the C═O, indicate the coordination of the carboxylate ligands with the iron sites in the framework. The band at 1450 cm^{-1} is related to the ν(OH) flexural vibrations. The spectra of MIL-100(Fe) also display two sharp bands at 760 and 710 cm^{-1}, attributed to the C−H stretching vibrations of the benzene rings.[32] The band at 620 cm^{-1} is assigned to the $\nu(Fe_3O)$ vibration. Finally, the typical band of unreacted BTC at 1710 cm^{-1} was negligible, indicating that purification was successful with regard to removing the unreacted ligand.[33−35] N_2 adsorption resulted in a BET surface area of 1450 ± 60 m^2/g for nanoMOFs (RT) and 1720 ± 40 m^2/g for nanoMOFs (MW), respectively, in line with previously reported data.[36,37]

Degradation of NanoMOFs through Ex Situ Methods. NanoMOFs (MW) were allowed to degrade in acidic (pH 5.4) or neutral (pH 7.4) PBS at 37 °C. The pH corresponds to physiological conditions (7.4) and to more acidic ones (5.4), corresponding to intracellular endosomal compartments and to diseased sites.[16] An incubation time of 48 h was chosen to ensure maximal degradation, according to previously published data.[18,19,38,39] The degraded nanoparticles were thoroughly purified by washing to remove salts and were then investigated by STEM-HAADF to evaluate their morphological and dimensional changes (Figure S1).

NanoMOFs (MW) incubated in acidic PBS maintained their faceted crystalline structures, as shown by the presence of well-defined crystalline planes (Figure 2b) and FFT patterns (Figure 2c). On the contrary, after exposure to neutral PBS, the nanoparticles' crystallinity was rapidly lost, and the crystalline planes disappeared in favor of an amorphous structure with a random porosity (Figure 2d,e). Interestingly, despite losing more than 90% of their constitutive trimesate ligand, the nanoMOFs' (MW) mean diameter changes were only around 11% [140 ± 37 nm (in H_2O) and 125 ± 11 nm after degradation in PBS], in agreement with previous studies.[3,18,19,39]

STEM-HAADF-EDX allowed further information to be gained about the degradation mechanism. Advantageously, it allows mapping of the distribution of the nanoMOFs' (MW) constitutive elements: Fe, C, and O from the framework structure and P from the coordinative interaction with PBS. It should be mentioned that although the nanoparticles' trimesate constitutive ligand consists of C and O atoms, tracking these elements is not a good option for STEM-HAADF-EDX studies. Indeed, sample holders contain C, making it difficult to separate information arising from C atoms in the grids from the analyzed samples. Besides, nanoMOFs contain a non-negligible amount of coordinated water molecules, which cannot be removed even under high vacuum conditions.

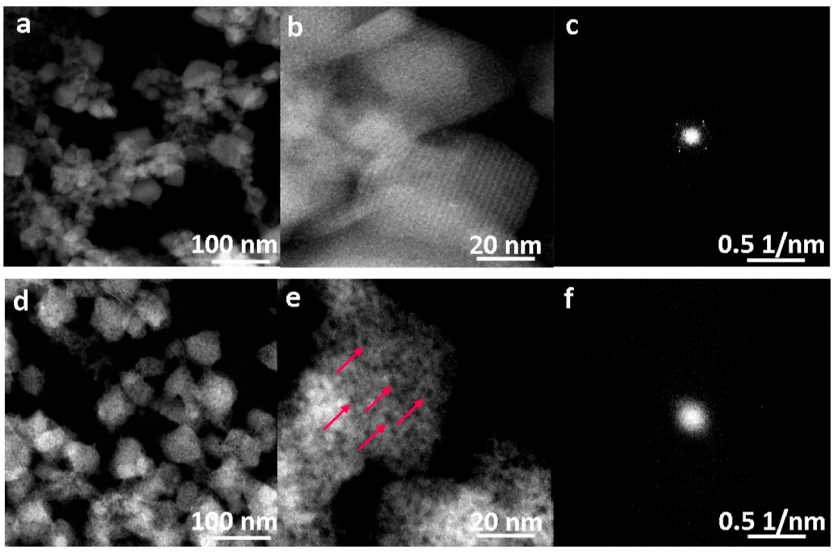

Figure 2. (a,b) STEM-HAADF images of nanoMOFs (MW) after 48 h of degradation in PBS at pH 5.4 and (d,e) in PBS at pH 7.4. The concentration was 0.25 mg mL^{-1}. Red arrows show the appearance of large pores (red arrows) indicating degradation. (c,f) FFT patterns of degraded nanoMOFs (MW) indicate the loss of crystallinity.

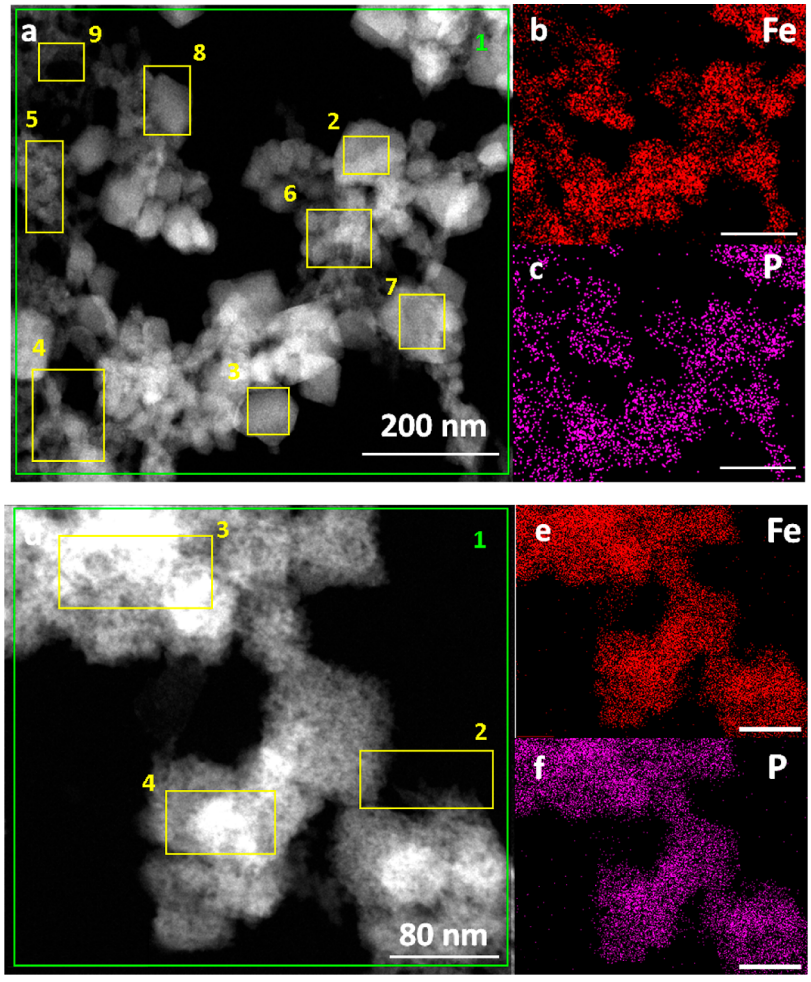

Figure 3. (a,d) STEM-HAADF images of nanoMOFs (MW) after 48 h of incubation in PBS at pH 5.4 and pH 7.4, respectively. (b,c,e,f) Elemental analysis reveals the homogeneous distribution of P after degradation. Yellow and green rectangles represent the selected regions by STEM-HAADF-EDX.

Therefore, information on O distribution arises both from coordinated water and trimesate ligands (Figure S5).

On the other hand, the atomic P/Fe ratio brings valuable insights into the evolution of the chemical composition due to

degradation in PBS. It is worth noting that Fe remains associated with the nanoMOFs (MW) all over the degradation process as no Fe was detected in the PBS release media at pH 7.4.[3,18] On the contrary, phosphate ions from PBS progressively penetrate inside the matrix and coordinate with the iron sites.[19,39] Therefore, determining the atomic P/Fe ratio is indicative of the nanoMOFs' degradation.

Thus, our attention was focused on the quantification of the Fe and P atoms. First, the distribution of P atoms within the nanoMOFs was homogeneous. In Figure 3a,d, the selected regions of interest for the quantification of the elements are represented by yellow rectangles, while the green one represents the integral region (numbered 1). The normalized atomic percentage (at. %) of P was calculated for each region. In the case of incubation in acidic PBS (Figure 3a), the median calculated P (at. %) was 2.4 ± 0.7. In contrast, for neutral environments, P (at. %) was as high as 7.4 ± 0.5. These results show that P is evenly distributed with a much higher % in the case of pH = 7.4. Second, the P/Fe atomic ratios were calculated for multiple regions of the nanoMOFs (MW). The P/Fe ratio was found to be almost three times lower for particles degraded at pH 5.4 than for those degraded at pH 7.4 (0.3 ± 0.1 as compared to 0.7 ± 0.4.) (Figure 3). In a nutshell, these results suggest the lower degradation of the nanoMOFs (MW) under acidic conditions as compared to neutral ones.

In addition, we took advantage of the STEM-HAADF methodology to assess the local P/Fe ratios and confirm that the degradation of the studied nanoMOFs (MW) was complete after 48 h (pH = 7.4). Indeed, after 72 h of degradation, the P/Fe ratio remained stable (0.7 ± 0.4) and similar morphologies were obtained to those at 48 h (Figure S6).

To complete the study, the amount of BTC ligand released from nanoMOFs (RT) and nanoMOFs (MW) upon incubation in acidic and neutral PBS was measured at different time points by HPLC. In agreement with STEM-HAADF-EDX investigations, the nanoMOFs (MW) progressively released their constitutive ligand in neutral PBS. The amounts of released BTC were 76 ± 7, 95 ± 8, and 100 ± 3 wt % after 1.5, 6, and 24 h, respectively, whereas under acidic conditions (pH 5.4), the degradation kinetics was much slower and partial, with 23 ± 1, 30 ± 1, and 38 ± 1 wt % BTC loss at the same time points.

To further assess the stability of the nanoMOFs (MW) in pure water, trimesate release also followed upon nanoparticle storage. After 2 days of incubation, less than 2 wt % of the ligand was lost. This negligible loss could probably correspond to the unreacted residual ligand that remained trapped in the nanoMOF pores after their synthesis. Interestingly, whatever the synthesis method (RT or MW), similar degradation patterns were observed, suggesting that whatever their size, the nanoMOFs were stable in water (Figure 4). Another important point was the fast ligand release in the first minutes after the start of the degradation studies in both acidic and neutral PBS (40 ± 2 and 12 ± 1 wt %, respectively). This suggests that the degrading phosphate ions from PBS diffuse fast inside the nanoMOFs, coordinate with the unsaturated iron site, and lead to ligand displacement.

As previously reported, MIL-100(Fe) particles were found to be more stable in acidic environments as compared to neutral ones.[39] This observation can be explained by the complexation of the phosphate ions with the iron metal sites of the framework. In PBS at pH = 7.4, $H_2PO_4^-$ and HPO_4^{2-}

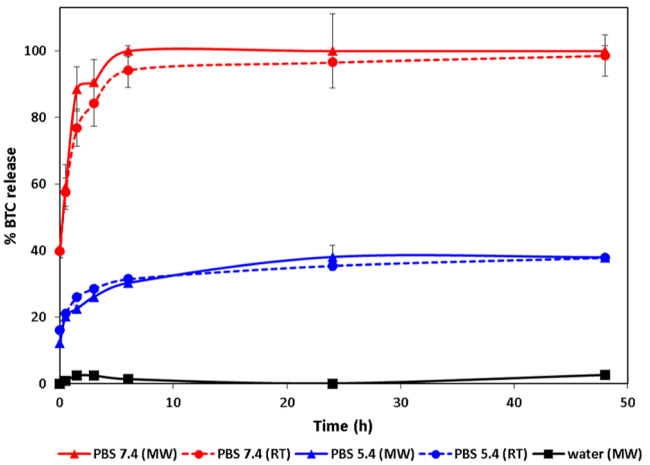

Figure 4. Trimesate release during nanoMOFs' incubation in PBS (pH 7.4 and 5.4) and in water evaluated by HPLC. The sample concentration was 0.5 mg mL^{-1}.

species are in equilibrium at a similar concentration (5 mM). On the other hand, in the range of pH = 4−6, $H_2PO_4^-$ anions are predominant compared to HPO_4^{2-} (99:1 at pH 5.4). At both studied pH values, 5.4 and 7.4, phosphate ions diffuse into the nanoMOF porosity and coordinate with the iron sites. By looking at the speciation diagram of Fe(III) in water, we observe that it is very poorly soluble at pH 7.4 [the pH at which $Fe(OH)_3$ precipitates] and slightly soluble at pH 5.4, mostly as $Fe(OH)^{2+}$ monocations.[40] This fact cannot explain the faster degradation at pH 7.4 of nanoMOFs. As a consequence, the faster dissolution probably comes from the superior chelating strength of the HPO_4^{2-} anion for iron centers, which replaces carboxylate functions of the nanoMOFs.

An additional indication of the nanoMOFs' degradation was the change in their surface charge, related to their ζ-potential values. The initial positive ζ-potential value for nondegraded nanoMOFs (MW) dispersed in H_2O (+26 ± 2.1 mV) dramatically changed to negative after 24 h of degradation (−15 ± 1.3 and −37 ± 2.1 mV in PBS 5.4 and 7.4, respectively). This could be explained by the coordination of the phosphate ions with the unsaturated iron sites at the external surface of the nanoMOFs and is in line with previously reported studies.[18]

In agreement with these findings, a rapid loss of crystallinity was observed upon degradation in PBS, as shown by the PXRD patterns of nano-MOFs (Figure S7). After only 1 h in neutral PBS, the crystallinity was totally lost, whereas in acidic PBS, the main characteristic Bragg peaks of MIL-100(Fe) were still observed after 2 days of incubation. This clearly shows that the structure was more stable at pH 5.4 than at pH 7.4.

Moreover, FT-IR spectroscopy showed changes in the chemical composition of the nanoMOFs upon 48 h of incubation in PBS (Figure S8). Whatever the pH, a broad band at 1050 cm^{-1} was observed, corresponding to asymmetrical P−O stretching.[41,42] In a more acidic environment (PBS 5.4), the intensity of the stretching bands at 1380 and 1640 cm^{-1}, corresponding to the symmetric and asymmetric vibrations of the trimesate, slightly decreased. Thus, it can be concluded that nanoMOFs maintained their composition to a high extent, in agreement with the STEM-HAADF results. However, in neutral PBS, the typical bands of the ligand were either broadened (1380 and 1450 cm^{-1}) or disappeared (1640,

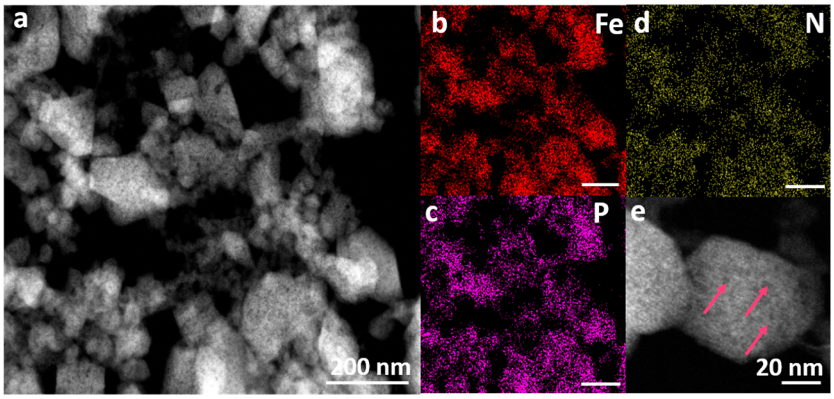

Figure 5. (a,e) STEM-HAADF images of nanoMOFs (MW) after 48 h of incubation in PBS−BSA at pH = 7.4 (0.25 mg mL^{-1}). The formation of "holes" represented by pink arrows suggests the degradation of the particles. (b−d) STEM-HAADF-EDX elemental analysis of Fe, P, and N of nanoMOFs (MW).

760, and 710 cm^{-1}), suggesting the substantial release of the ligand and, consequently, the formation of amorphous degraded nanoMOFs. These observations are in line with the massive trimesate loss at pH 7.4, as quantified by HPLC (Figure 4).

The N_2 adsorption isotherms for the degraded nanoMOFs (MW) revealed a strong decrease in their surface area upon degradation (Figure S9), which correlates with the loss of the trimesate constitutive ligand due to the phosphatation of the framework. The initial BET surface area (1720 ± 40 m^2/g) decreased to 960 ± 20 and 200 ± 40 m^2/g for nanoMOFs degraded in PBS at pH 5.4 and 7.4, respectively.

To conclude, nanoMOF particles partially lost their crystalline structure in PBS, depending on the acidity of the medium. In a complementary study, PBS solution (pH 7.4) was enriched with BSA (3.7% w/v) to investigate its contribution to the degradation mechanism of nanoMOFs.

Degradation of NanoMOFs in the Presence of Protein. NanoMOFs (MW) were immersed in neutral PBS containing BSA at a concentration corresponding to the standard one in blood.[37] Figure 5 presents the morphology and the distribution of elements (Fe, P, and N) as observed by STEM-HAADF-EDX after 48 h of incubation at 37 °C. Of interest, nitrogen mapping is indicative of the location of BSA as this element is only present in the protein.

NanoMOFs (MW) kept their faceted structures (Figure 5a,e) and some of the initial crystalline planes (Figure 5e), but "holes" in their structure similar to those observed in PBS 7.4 without BSA (Figure 2e) also appeared (Figure 5e). Figure 5d shows an even distribution of N (from BSA), which coincides with the location of the nanoparticles, suggesting that they were homogeneously covered by this protein (the N/Fe ratio was found at 0.5 ± 0.3) after 48 h of degradation. This is in line with data in the literature, showing that albumin readily adsorbs on nanoMOFs (MW).[37,43] However, in our case, the presence of BSA did not impede the nanoMOF degradation in PBS, as indicated by the high amounts of phosphorus (and thus phosphates) found in the degraded samples (Figure 5c). Indeed, calculated P/Fe ratios were 0.7 ± 0.3, similar to the ones found in the case of nanoMOF degradation in PBS 7.4 without BSA (0.5 ± 0.3). Most likely, BSA formed a noncompact corona around the external surface, leaving free pathways to the phosphate ions to diffuse in the core of the particles. To gain a further understanding of the degradation process, constitutive trimesate loss was comparatively followed by HPLC in the case of nanoMOFs (MW) incubated in PBS with and without BSA. The presence of BSA on the surface of nanoMOFs led to a slight decrease in degradation kinetics for the short times until the total degradation (24 h) (Figure S10). This suggests that the protein corona slows down the nanoparticles' degradation, but it does not impede the phosphates' diffusion, which is in agreement with STEM-HAADF results.

To sum up, nanoMOFs, whatever their size, degrade under simulated physiological conditions by releasing practically the total amount of their constitutive ligand, regardless of the presence of BSA in the degradation medium due to the rapid diffusion of phosphate ions in their porous structure. However, nanoMOFs globally maintained their shape despite a dramatic change in their composition.

These findings prompted us to explore the nanoMOFs' degradation under extremely diluted conditions, by in situ ellipsometry. To do so, nanoMOFs were deposited onto a silicone surface, forming thin layers assimilated to films. It is worth noting that in situ ellipsometry is a sensitive technique, allowing us to gain insights into the compositional changes underway in nanoMOFs upon their degradation while avoiding the constraints of saturation and aggregation that occur under bulk conditions.

In the first step, thin films were prepared and studied under well-controlled conditions of temperature and flow.

Thin Film Characterization. The thin films of optical quality were successfully prepared using an ethanolic formulation of nanoMOFs (RT) by a dip-coating process. As observed by SEM (Figure 6), the films are made of stacks of small MOFs' aggregates. Indeed, similar voids have also been reported for silicon substrates coated with other types of nanoparticles.[26] Although the size of these aggregates impedes the formation of a homogeneous film, the obtained coating scatters very little light once it is soaked in water, enabling the in situ ellipsometrical measurements. Indeed, during in situ ellipsometrical measurements, we observed no light depolarization, proving that in these conditions, MOFs' films have good optical quality.

The film thickness and refractive index were determined in the visible region by SE, as described in Section 2.5. The mean film thickness was measured at 200 ± 20 nm on 10 films. The reproducibility of the films enabled further studies by in situ ellipsometry to compare their degradation under various conditions.

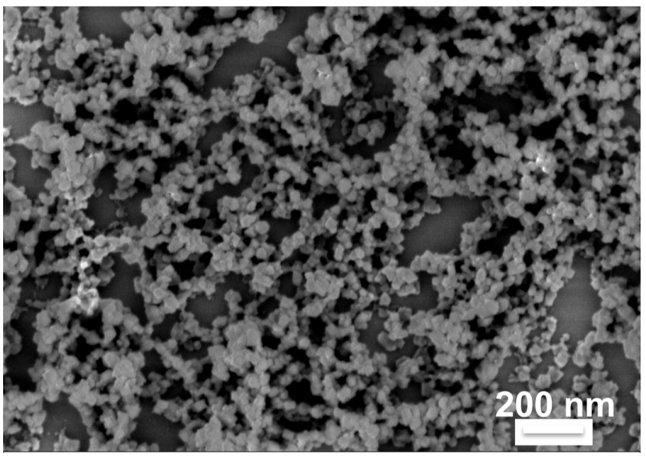

Figure 6. SEM images of nanoMIL-100(Fe) (RT) thin films.

In Situ Ellipsometry. First, films were incubated in water, where very limited evolution occurred (Figure S11a). Indeed, the film thickness was reduced by only 1.5% after 200 min. This limited modification correlates well with the HPLC [illegible] suggesting a good nanoMOF chemical stability in water. Similar results were obtained in PBS at pH = 5.4 with a thickness decrease of about 3% after 200 min. By contrast, a rapid mean thickness decrease of 5−6% was observed as soon as the films were soaked in PBS solution at pH = 7.4. The colloidal layer tended to stabilize after about 100 min (Figure S11b,c). These data support the rapid structural evolution of nanoMOFs (RT) described in the first part of this article.

Second, studies were carried out in PBS enriched in BSA, as was done previously. At early times (less than 1 h), the film thickness calculated by in situ ellipsometry follows the same tendency as that in PBS at pH = 7.4 devoid of BSA. Then, a constant increase in the thickness was measured, most likely related to the adsorption of protein onto the particles' surface (Figure S11d), which seems favored after 75 min, after the formation of a phosphate-rich layer on nanoMOFs' particles.

Changes in the thicknesses of the films certainly give us a strong indication of possible changes in the nanoMOF (RT) structure upon degradation but cannot prove their chemical transformation. The resulting values can be attributed only to a mechanical contraction of the film or a physical rearrangement of the colloids to achieve better stacking due to the constant flow of the liquid media. Thus, to gain further insights, we determined the imaginary part of the refractive index (extinction coefficient k), which quantifies the absorption of electric waves propagating within the films. This parameter is proportional to the light absorption coefficient and is indicative of modifications of the electronic environment of the iron metal. UV−vis diffuse reflectance of the original nanoMOF (RT) powder presents two absorption peaks at 440 and 540 nm, while that of the totally transformed material presents only one absorption shoulder at 440 nm followed by a smooth absorption decrease with increasing wavelength (Figure S12). By this technique, it is impossible to follow in situ the evolution of the UV−vis spectra. The advantage of the ellipsometric measurement is that one can follow the same region of interest and amount of matter with no need to use normalization procedures (such as the Kuberka−Munk data treatment used for powder absorption analyses, for example). This approach does not suffer from the usual preparation bias of powders (grinding homogeneity of the powder, dispersion quality of grains within $BaSO_4$, etc.) that makes the estimation of the absolute absorption amplitude (thus the comparison of powders) sometimes difficult.

When analyzing in situ the degradation of nanoMOFs, we followed by visible ellipsometry the evolution of the extinction coefficient k as a function of time. By modeling the absorption band centered at 540 nm, the evolution of k at 540 nm in different environments could be observed (Figure 7). This

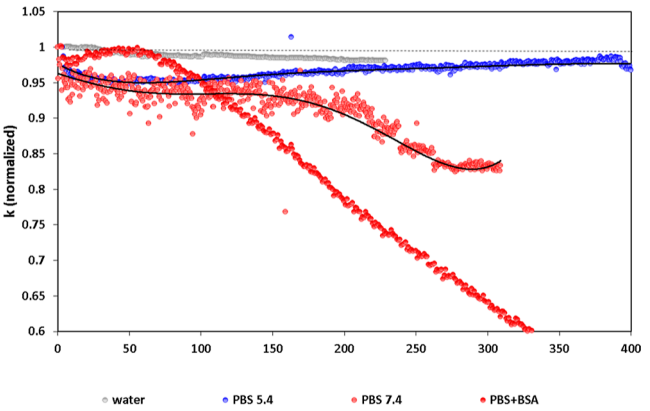

Figure 7. Evolution of the extinction coefficient at 540 nm, normalized at t = 0 and, taking into account the film thickness variations, calculated by in situ ellipsometry for nanoMOF (RT) film incubated in water (orange), PBS 5.4 (yellow), PBS 7.4 (gray), and PBS 7.4 containing BSA (blue). Fitted polynomes were superimposed onto PBS 5.4 and PBS 7.4 curves for easing their discrimination. They are only guides for the eyes.

experimental approach measures the optical properties of nanoMOF films per unit volume. This offers the immense advantage of taking into account and compensating for the possible film thickness variations due to particle packing during experiments.

After normalization of the extinction coefficients, it was found that nanoMOFs (RT) on their support exhibited very little evolution in water. On the contrary, an immediate drop in k in the first 5−10 min in PBS at pH 7.4 was noticed. This fast response of optical absorption witnesses the formation of iron phosphate species that are known to have no discrete absorption band at 540 nm wavelength.[44] As a consequence, this is likely due to the rapid chemisorption of phosphate anions on iron centers.

The extinction coefficients measured in different media diverged progressively over time (Figure 7). At pH 5.4, the k values progressively converged through the k curve of colloids in water and then stabilized, meaning that no drastic change seems to occur after an initial fast transformation. In contrast, at pH 7.4, k values exhibited a slow decrease from 40 to around 140 min, followed by a drastic decrease. This is an indication of a progressive structural transformation taking place in the immediate environment of iron sites. As most of the ligand is released after 2 h (about 70−80%, Figure 4), the fast optical transformation observed after 140 min may be related to the final displacement of trimesate ligands from the coordination sphere of iron centers, allowing a local rearrangement of the iron centers and phosphate anions.

Finally, in the presence of BSA, a moderate evolution of k during the first hour was noted. No sign of short-term phosphate adsorption is visible in that case. Then a rapid

acceleration of optical transformation, which reaches a k decrease rate similar to that of pure PBS 7.4, was observed. This last point suggests that PBS does not significantly change the final transformation rate of the colloids, in agreement with the ex situ studies previously discussed in this study for the degradation of nanoMOFs (MW) (STEM-HAADF, EDX, HPLC, PXRD, and FT-IR).

Characterization of the Degraded Films. After the degradation mechanism of the thin films was explored by in situ ellipsometry, IR spectroscopy was further applied to gain additional information on their chemical composition (Figure 8). To note, the films incubated in PBS were washed three

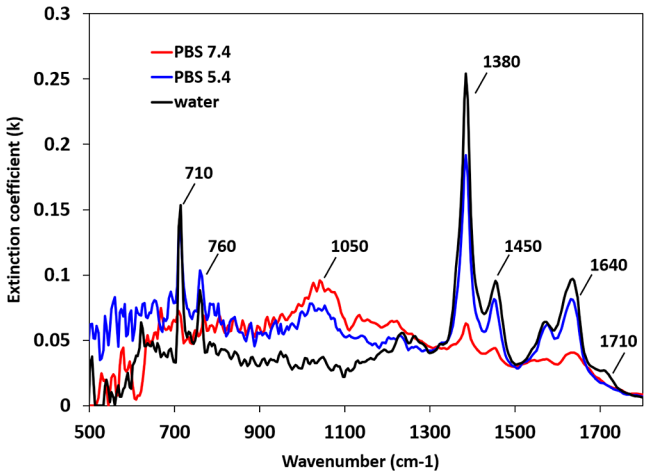

Figure 8. Infrared spectra of films after in situ measurements in water (black), PBS 5.4 (blue), and PBS 7.4 (red).

times in Milli-Q water to remove the excess of the remaining salts, which could recrystallize on the surface during the drying process.

Upon incubation in aqueous media, where no degradation occurred, the spectrum of nanoMOFs (RT) with the typical bands of the carbonyl group of the ligand coordinating with the iron sites of the framework was obtained. This spectrum is a strong indication of the successful coating of the substrate with nanoparticles as well as its stability upon incubation in water. When the film was in contact with PBS 5.4 (more than 2 h), a new band appeared at around 1050 cm^{-1}, denoting the anchoring of the phosphate ions within the framework. As for the FT-IR of nanoMOFs (MW) before deposition (Figure S8), typical bands of the carboxylate ligand were still found, showing that the vibrational structure of the MOFs remained mostly intact in this acidic environment in the presence of phosphate ions, even after 2 days of incubation. In the case of neutral PBS, where a fast degradation was observed, IR spectroscopy was applied to a film that was in contact with PBS 7.4 for only 5 min. This time point was selected to study the influence of phosphates on the degradation mechanism of nanoMOFs (RT) at short times. Indeed, the band at 1050 cm^{-1}, corresponding to P−O stretching, was found.[45] It is worth noting that the typical carbonyl bands of trimesate at 1380, 1450, and 1640 cm^{-1} severely decreased, designating the quasi-instant chemical transformation of nanoparticles.

To conclude, both the evolution of the extinction coefficient k and the IR spectroscopy of the films showed fast chemical changes in the nanoparticles occurring within a few minutes, depending on the degradation media. Based on these results, degradation kinetics following a two-step mechanism can be proposed; first, an almost instant fixation of phosphates to the iron centers of the matrix, and a slower second step, where the organic trimesate ligand is progressively substituted by the phosphates.

CONCLUSION

The degradation of nanoMOFs in extremely diluted conditions mimicking their intravenous administration has been scrutinized by using a series of complementary characterization methods. Special emphasis was put on ex situ studies by STEM-HAADF microscopy, and for the first time, an in situ IR ellipsometry method was used. NanoMOFs were deposited on silicon wafers, resulting in thin films of high optical quality. Remarkably, nanoMOFs adhered onto the wafers during the experiments, allowing the detection of any thickness or compositional change occurring as soon as the particles came in contact with various media.

From these advanced characterization techniques, a two-step degradation mechanism was proposed: a fast first step, where phosphate ions diffused in the framework and adsorbed very quickly onto iron centers (within 5 min), and a slow second step, leading to the progressive displacement of the constitutive trimesate ligands, leading to structural transformation. It was also found that the degradation process was pH-dependent and that nanoMOF particles were readily degraded under neutral conditions. On the contrary, the nanoparticles partially maintained their global chemical composition in acidic conditions, despite the incorporation of phosphates in their internal porosity. Finally, the presence of a protein coating layer did not impede the degradation process, suggesting that

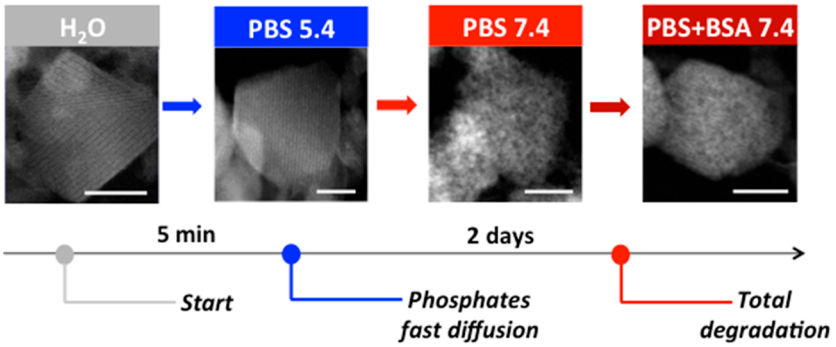

Figure 9. STEM-HAADF images of nanoMOF particles upon incubation in water, under acidic conditions (PBS 5.4), under neutral conditions (PBS 7.4), and in the presence of BSA protein (3.7% w/v). In all cases, incubations were performed at 37 °C for 48 h. Scale bars represent 20 nm.

the internal porosity of the nanoMOFs was still permeable by the phosphate ions (Figure 9).

The methodology presented here paves the way for numerous possible applications, such as the study of nanoMOFs' degradation in more complex media such as serum and blood. In future studies, it could be intriguing to further investigate the degradation mechanism of nanoMOFs as a function of their coating. Indeed, a variety of materials (functionalized polymers, lipids, and cyclodextrins) were used to functionalize the nanoMOFs.[16,46] It will be of interest to determine if some of these coatings could influence the nanoMOF core (loaded or not with drugs) degradation. It has been shown that certain drugs such as topotecan stabilize the nanoMOFs toward degradation.[10] Therefore, it will be important to study their degradation mechanism in situ by the method that has been set up to better understand the influence of loaded drugs and coatings.

ASSOCIATED CONTENTS

The Supporting Information is available free of charge at https://pubs.acs.org/doi/10.1021/acsami.3c18958.

Characterization results of nondegraded nanoMOFs: DLS, SEM, STEM-HAADF, PXRD, and FT-IR; STEM-HAADF and elemental mapping of degraded nanoMOFs upon incubation in PBS 7.4; comparison of nondegraded and degraded nanoMOFs under acidic and neutral conditions (PBS 5.4 and 7.4): PXRD, FT-IR, and N_2 adsorption; trimesate release in the presence of BSA, followed by HPLC; films' thickness evaluation by in situ ellipsometry in different media; and solid-state UV−vis spectra of nondegraded and degraded nanoMOFs (PDF)

Author Contributions

The manuscript was written through contributions of all authors. C.B., I.C., and R.G. conceived the idea and designed the experiments. I.C. synthesized and characterized the materials. I.C. and C.B. performed the ellipsometric experiments. G.P. and I.C. performed and analyzed STEM-HAADF-EDX experiments. C.B., I.C., and R.G. collected and analyzed data. All authors participated in the data discussion. C.B., I.C., and R.G. wrote the manuscript, and all authors revised the manuscript. All authors have approved the final version of the manuscript.

Funding

This research was funded by the Paris Ile-de-France Region—DIM Respore, grant number "LS 167151". This work was supported by a public grant overseen by the French National Research Agency (ANR) as part of the "Investissements d'Avenir" program (Labex NanoSaclay, reference: ANR-10-LABX-0035).

Notes

The authors declare no competing financial interest.

AKNOWLEDGMENTS

We are grateful to Dr. Antoine Tissot for help with solid UV−vis spectroscopy and to Dr. Farid Nouar for the synthesis of nanoMIL-100 (Fe) at RT. We acknowledge Dr. Francois Brisset for SEM microscopy. I.C. thanks the Paris Ile-de-France Region—DIM Respore for a Ph.D. fellowship.

REFERENCES

(1) Langer, R.; Folkman, J. Polymers for the Sustained Release of Proteins and Other Macromolecules. *Nature* **1976**, *263* (5580), 797−800.

(2) Mitchell, M. J.; Billingsley, M. M.; Haley, R. M.; Wechsler, M. E.; Peppas, N. A.; Langer, R. Engineering Precision Nanoparticles for Drug Delivery. *Nat. Rev. Drug Discovery* **2021**, *20*, 101−124.

(3) Horcajada, P.; Chalati, T.; Serre, C.; Gillet, B.; Sebrie, C.; Baati, T.; Eubank, J. F.; Heurtaux, D.; Clayette, P.; Kreuz, C.; Chang, J. S.; Hwang, Y. K.; Marsaud, V.; Bories, P. N.; Cynober, L.; Gil, S.; Férey, G.; Couvreur, P.; Gref, R. Porous Metal-Organic-Framework Nanoscale Carriers as a Potential Platform for Drug Delivery and Imaging. *Nat. Mater.* **2010**, *9* (2), 172−178.

(4) Qiu, J.; Li, X.; Gref, R.; Vargas-Berenguel, A. Carbohydrates in Metal Organic Frameworks: Supramolecular Assembly and Surface Modification for Biomedical Applications. *Metal-Organic Frameworks for Biomedical Applications*; Elsevier Inc., 2020.

(5) Ploetz, E.; Engelke, H.; Lächelt, U.; Wuttke, S. The Chemistry of Reticular Framework Nanoparticles: MOF, ZIF, and COF Materials. *Adv. Funct. Mater.* **2020**, *30* (41), 1909062.

(6) Baati, T.; Njim, L.; Neffati, F.; Kerkeni, A.; Bouttemi, M.; Gref, R.; Najjar, M. F.; Zakhama, A.; Couvreur, P.; Serre, C.; Horcajada, P. In Depth Analysis of the in Vivo Toxicity of Nanoparticles of Porous Iron(III) Metal-Organic Frameworks. *Chem. Sci.* **2013**, *4* (4), 1597−1607.

(7) Simon-Yarza, T.; Baati, T.; Neffati, F.; Njim, L.; Couvreur, P.; Serre, C.; Gref, R.; Najjar, M. F.; Zakhama, A.; Horcajada, P. In Vivo Behavior of MIL-100 Nanoparticles at Early Times after Intravenous Administration. *Int. J. Pharm.* **2016**, *511* (2), 1042−1047.

(8) Simon-Yarza, T.; Mielcarek, A.; Couvreur, P.; Serre, C. Nanoparticles of Metal-Organic Frameworks: On the Road to In Vivo Efficacy in Biomedicine. *Adv. Mater.* **2018**, *30* (37), 1707365.

(9) Anand, R.; Borghi, F.; Manoli, F.; Manet, I.; Agostoni, V.; Reschiglian, P.; Gref, R.; Monti, S. Host-Guest Interactions in Fe(III)-Trimesate MOF Nanoparticles Loaded with Doxorubicin. *J. Phys. Chem. B* **2014**, *118* (29), 8532−8539.

(10) Di Nunzio, M. R.; Agostoni, V.; Cohen, B.; Gref, R.; Douhal, A. A "Ship in a Bottle" Strategy to Load a Hydrophilic Anticancer Drug

in Porous Metal Organic Framework Nanoparticles: Efficient Encapsulation, Matrix Stabilization, and Photodelivery. *J. Med. Chem.* **2014**, *57* (2), 411−420.
(11) Rodriguez-Ruiz, V.; Maksimenko, A.; Anand, R.; Monti, S.; Agostoni, V.; Couvreur, P.; Lampropoulou, M.; Yannakopoulou, K.; Gref, R. Efficient "Green" Encapsulation of a Highly Hydrophilic Anticancer Drug in Metal-Organic Framework Nanoparticles. *J. Drug Targeting* **2015**, *23* (7−8), 759−767.
(12) Li, X.; Semiramoth, N.; Hall, S.; Tafani, V.; Josse, J.; Laurent, F.; Salzano, G.; Foulkes, D.; Brodin, P.; Majlessi, L.; Ghermani, N. E.; Maurin, G.; Couvreur, P.; Serre, C.; Bernet-Camard, M. F.; Zhang, J.; Gref, R. Compartmentalized Encapsulation of Two Antibiotics in Porous Nanoparticles: An Efficient Strategy to Treat Intracellular Infections. *Part. Part. Syst. Charact.* **2019**, *36* (3), 1−9.
(13) Tamames-Tabar, C.; Cunha, D.; Imbuluzqueta, E.; Ragon, F.; Serre, C.; Blanco-Prieto, M. J.; Horcajada, P. Cytotoxicity of Nanoscaled Metal-Organic Frameworks. *J. Mater. Chem. B* **2014**, *2* (3), 262−271.
(14) Grall, R.; Hidalgo, T.; Delic, J.; Garcia-Marquez, A.; Chevillard, S.; Horcajada, P. In Vitro Biocompatibility of Mesoporous Metal (III; Fe, Al, Cr) Trimesate MOF Nanocarriers. *J. Mater. Chem. B* **2015**, *3* (42), 8279−8292.
(15) Wuttke, S.; Zimpel, A.; Bein, T.; Braig, S.; Stoiber, K.; Vollmar, A.; Müller, D.; Haastert-Talini, K.; Schaeske, J.; Stiesch, M.; Zahn, G.; Mohmeyer, A.; Behrens, P.; Eickelberg, O.; Bölükbas, D. A.; Meiners, S. Validating Metal-Organic Framework Nanoparticles for Their Nanosafety in Diverse Biomedical Applications. *Adv. Healthcare Mater.* **2017**, *6* (2), 1600818.
(16) Ding, M.; Liu, W.; Gref, R. Nanoscale MOFs: From Synthesis to Drug Delivery and Theranostics Applications. *Adv. Drug Delivery Rev.* **2022**, *190*, 114496.
(17) Ettlinger, R.; Lächelt, U.; Gref, R.; Horcajada, P.; Lammers, T.; Serre, C.; Couvreur, P.; Morris, R. E.; Wuttke, S. Toxicity of Metal-Organic Framework Nanoparticles: From Essential Analyses to Potential Applications. *Chem. Soc. Rev.* **2022**, *51*, 464.
(18) Bellido, E.; Guillevic, M.; Hidalgo, T.; Santander-Ortega, M. J.; Serre, C.; Horcajada, P. Understanding the Colloidal Stability of the Mesoporous MIL-100(Fe) Nanoparticles in Physiological Media. *Langmuir* **2014**, *30* (20), 5911−5920.
(19) Li, X.; Lachmanski, L.; Safi, S.; Sene, S.; Serre, C.; Grenèche, J. M.; Zhang, J.; Gref, R. New Insights into the Degradation Mechanism of Metal-Organic Frameworks Drug Carriers. *Sci. Rep.* **2017**, *7* (1), 13142.
(20) Christodoulou, I.; Lyu, P.; Soares, C. V.; Patriarche, G.; Serre, C.; Maurin, G.; Gref, R. Nanoscale Iron-Based Metal-Organic Frameworks: Incorporation of Functionalized Drugs and Degradation in Biological Media. *Int. J. Mol. Sci.* **2023**, *24* (4), 3362.
(21) Wright, A. K.; Thompson, M. R. Hydrodynamic Structure of Bovine Serum Albumin Determined by Transient Electric Birefringence. *Biophys. J.* **1975**, *15* (2), 137−141.
(22) Sene, S.; Marcos-Almaraz, M. T.; Menguy, N.; Scola, J.; Volatron, J.; Rouland, R.; Grenèche, J. M.; Miraux, S.; Menet, C.; Guillou, N.; Gazeau, F.; Serre, C.; Horcajada, P.; Steunou, N. Maghemite-NanoMIL-100(Fe) Bimodal Nanovector as a Platform for Image-Guided Therapy. *Chem* **2017**, *3* (2), 303−322.
(23) Simon-Yarza, T.; Giménez-Marqués, M.; Mrimi, R.; Mielcarek, A.; Gref, R.; Horcajada, P.; Serre, C.; Couvreur, P. A Smart Metal-Organic Framework Nanomaterial for Lung Targeting. *Angew. Chem., Int. Ed.* **2017**, *56* (49), 15565−15569.
(24) Rojas, S.; Colinet, I.; Cunha, D.; Hidalgo, T.; Salles, F.; Serre, C.; Guillou, N.; Horcajada, P. Toward Understanding Drug Incorporation and Delivery from Biocompatible Metal-Organic Frameworks in View of Cutaneous Administration. *ACS Omega* **2018**, *3* (3), 2994−3003.
(25) Bhattacharjee, S. DLS and zeta potential-What they are and what they are not? *J. Controlled Release* **2016**, *235*, 337−351.
(26) Fontecave, T.; Sanchez, C.; Azaïs, T.; Boissière, C. Chemical Modification as a Versatile Tool for Tuning Stability of Silica Based Mesoporous Carriers in Biologically Relevant Conditions. *Chem. Mater.* **2012**, *24* (22), 4326−4336.
(27) Bindini, E.; Chehadi, Z.; Faustini, M.; Albouy, P. A.; Grosso, D.; Cattoni, A.; Chanéac, C.; Azzaroni, O.; Sanchez, C.; Boissière, C. Following in Situ the Degradation of Mesoporous Silica in Biorelevant Conditions: At Last, a Good Comprehension of the Structure Influence. *ACS Appl. Mater. Interfaces* **2020**, *12* (12), 13598−13612.
(28) Panchal, M.; Nouar, F.; Serre, C.; Benzaqui, M.; Sene, S.; Steunou, N.; Gimenez Marqués, M. Low Temperature Process For The Synthesis Of MOF Carboxylate Nanoparticles. EP 3357929 A1, 2017.
(29) Agostoni, V.; Horcajada, P.; Rodriguez-Ruiz, V.; Willaime, H.; Couvreur, P.; Serre, C.; Gref, R. 'Green' Fluorine-Free Mesoporous Iron(III) Trimesate Nanoparticles for Drug Delivery. *Green Mater.* **2013**, *1* (4), 209−217.
(30) García Márquez, A.; Demessence, A.; Platero-Prats, A. E.; Heurtaux, D.; Horcajada, P.; Serre, C.; Chang, J. S.; Férey, G.; De La Peña-O'Shea, V. A.; Boissière, C.; Grosso, D.; Sanchez, C. Green Microwave Synthesis of MIL-100(Al, Cr, Fe) Nanoparticles for Thin-Film Elaboration. *Eur. J. Inorg. Chem.* **2012**, *2012* (32), 5165−5174.
(31) Horcajada, P.; Surblé, S.; Serre, C.; Hong, D. Y.; Seo, Y. K.; Chang, J. S.; Grenèche, J. M.; Margiolaki, I.; Férey, G. Synthesis and Catalytic Properties of MIL-100(Fe), an Iron(III) Carboxylate with Large Pores. *Chem. Commun.* **2007**, *100* (27), 2820−2822.
(32) Mahalakshmi, G.; Balachandran, V. FT-IR and FT-Raman Spectra, Normal Coordinate Analysis and Ab Initio Computations of Trimesic Acid. *Spectrochim. Acta, Part A* **2014**, *124*, 535−547.
(33) Lv, H.; Zhao, H.; Cao, T.; Qian, L.; Wang, Y.; Zhao, G. Efficient Degradation of High Concentration Azo-Dye Wastewater by Heterogeneous Fenton Process with Iron-Based Metal-Organic Framework. *J. Mol. Catal. A: Chem.* **2015**, *400*, 81−89.
(34) Huang, S.; Yang, K. L.; Liu, X. F.; Pan, H.; Zhang, H.; Yang, S. MIL-100(Fe)-Catalyzed Efficient Conversion of Hexoses to Lactic Acid. *RSC Adv.* **2017**, *7* (10), 5621−5627.
(35) Leclerc, H.; Vimont, A.; Lavalley, J. C.; Daturi, M.; Wiersum, A. D.; Llwellyn, P. L.; Horcajada, P.; Férey, G.; Serre, C. Infrared Study of the Influence of Reducible Iron(Iii) Metal Sites on the Adsorption of CO, CO2, Propane, Propene and Propyne in the Mesoporous Metal-Organic Framework MIL-100. *Phys. Chem. Chem. Phys.* **2011**, *13* (24), 11748−11756.
(36) Simon, M. A.; Anggraeni, E.; Soetaredjo, F. E.; Santoso, S. P.; Irawaty, W.; Thanh, T. C.; Hartono, S. B.; Yuliana, M.; Ismadji, S. Hydrothermal Synthesize of HF-Free MIL-100(Fe) for Isoniazid-Drug Delivery. *Sci. Rep.* **2019**, *9* (1), 16907.
(37) Li, X.; Salzano, G.; Qiu, J.; Menard, M.; Berg, K.; Theodossiou, T.; Ladavière, C.; Gref, R. Drug-Loaded Lipid-Coated Hybrid Organic-Inorganic "Stealth" Nanoparticles for Cancer Therapy. *Front. Bioeng. Biotechnol.* **2020**, *8*, 1027.
(38) Cunha, D.; Ben Yahia, M.; Hall, S.; Miller, S. R.; Chevreau, H.; Elkaïm, E.; Maurin, G.; Horcajada, P.; Serre, C. Rationale of Drug Encapsulation and Release from Biocompatible Porous Metal-Organic Frameworks. *Chem. Mater.* **2013**, *25* (14), 2767−2776.
(39) Christodoulou, I.; Bourguignon, T.; Li, X.; Patriarche, G.; Serre, C.; Marlière, C.; Gref, R. Degradation Mechanism of Porous Metal-Organic Frameworks by in Situ Atomic Force Microscopy. *Nanomaterials* **2021**, *11* (3), 722.
(40) Baes, C. F.; Mesmer, R. S. *The Hydrolysis of Cations*; John Wiley & Sons: New York, London, Sydney, Toronto, 1976.
(41) Unamuno, X.; Imbuluzqueta, E.; Salles, F.; Horcajada, P.; Blanco-Prieto, M. J. Biocompatible Porous Metal-Organic Framework Nanoparticles Based on Fe or Zr for Gentamicin Vectorization. *Eur. J. Pharm. Biopharm.* **2018**, *132*, 11−18.
(42) Barnes, D. H.; Jugdaosingh, R.; Kiamil, S.; Best, S. M. Shelf Life and Chemical Stability of Calcium Phosphate Coatings Applied to Poly Carbonate Urethane Substrates. *J. Biotechnol. Biomater.* **2011**, *1* (06), 112.
(43) Cutrone, G.; Li, X.; Casas-Solvas, J. M.; Menendez-Miranda, M.; Qiu, J.; Benkovics, G.; Constantin, D.; Malanga, M.; Moreira-Alvarez, B.; Costa-Fernandez, J. M.; García-Fuentes, L.; Gref, R.;

Vargas-Berenguel, A. Design of Engineered Cyclodextrin Derivatives for Spontaneous Coating of Highly Porous Metal-Organic Framework Nanoparticles in Aqueous Media. *Nanomaterials* **2019**, *9* (8), 1103.
(44) Zhang, X. X.; Tang, S. S.; Chen, M. L.; Wang, J. H. Iron Phosphate as a Novel Sorbent for Selective Adsorption of Chromium(Iii) and Chromium Speciation with Detection by ETAAS. *J. Anal. At. Spectrom.* **2012**, *27* (3), 466−472.
(45) Ait Salah, A.; Jozwiak, P.; Zaghib, K.; Garbarczyk, J.; Gendron, F.; Mauger, A.; Julien, C. M. FTIR Features of Lithium-Iron Phosphates as Electrode Materials for Rechargeable Lithium Batteries. *Spectrochim. Acta, Part A* **2006**, *65* (5), 1007−1013.
(46) Cedrún-Morales, M.; Ceballos, M.; Polo, E.; del Pino, P.; Pelaz, B. Nanosized Metal-Organic Frameworks as Unique Platforms for Bioapplications. *Chem. Commun.* **2023**, *59* (20), 2869−2887.